

FOLLOWING THE COSMIC EVOLUTION OF PRISTINE GAS II: THE SEARCH FOR POP III-BRIGHT GALAXIES

RICHARD SARMENTO,¹ EVAN SCANNAPIECO,¹ AND SETH COHEN¹

¹*School of Earth and Space Exploration, Arizona State University, P.O. Box 871404, Tempe, AZ, 85287-1404*

ABSTRACT

Direct observational searches for Population III (Pop III) stars at high-redshift are faced with the question of how to select the most promising targets for spectroscopic follow up. To help answer this, we use a large-scale cosmological simulation, augmented with a new subgrid model that tracks the fraction of pristine gas, to follow the evolution of high-redshift galaxies and the Pop III stars they contain. We generate rest-frame ultraviolet (UV) luminosity functions for our galaxies and find that they are consistent with current $z \geq 7$ observations. Throughout the redshift range $7 \leq z \leq 16$ we identify ‘Pop III-bright’ galaxies as those with at least 75% of their flux coming from Pop III stars. While less than 5% of galaxies brighter than $m_{\text{UV,AB}} = 31.4$ mag are Pop III-bright between $7 \leq z \leq 8$, roughly a third of such galaxies are Pop III-bright at $z = 9$, right before reionization occurs in our simulation. Moving to $z = 10$, $m_{\text{UV,AB}} = 31.4$ mag corresponds to more luminous galaxies and the Pop III-bright fraction falls off to 15%. Finally at the highest redshifts, a large fraction of all galaxies are Pop III-bright regardless of magnitude. While $m_{\text{UV,AB}} = 31.4$ mag galaxies are likely not detectable during this epoch, we find 90% of galaxies at $z = 16$ are Pop III-bright with $m_{\text{UV,AB}} \leq 33$ mag, a lensed magnitude limit within reach of the James Webb Space Telescope. Thus we predict that the best redshift to search for luminous Pop III-bright galaxies is just before reionization, while lensing surveys for fainter galaxies should push to the highest redshifts possible.

Keywords: cosmology: theory, early universe – galaxies: high-redshift, evolution – stars: formation, Population III – luminosity function – turbulence

1. INTRODUCTION

Finding and characterizing the first galaxies is the next frontier in observational astronomy. Theoretical studies suggest that these metal-free stars could be observed today, if their initial mass function (IMF) extended to low masses (Scannapieco et al. 2006; Tumlinson 2006; Brook et al. 2007; Salvadori et al. 2010; Hartwig et al. 2015; Ishiyama et al. 2016). However, no one has yet observed a Population III (Pop III) star in or near the Galaxy (Christlieb et al. 2002; Cayrel et al. 2004; Aoki et al. 2006; Frebel et al. 2005; Norris et al. 2007; Caffau et al. 2011; Keller et al. 2014; Howes et al. 2015).

High-redshift observations have yielded candidates for Pop III stellar populations (Malhotra & Rhoads 2002; Dawson et al. 2004; Jimenez & Haiman 2006; Dijkstra & Wyithe 2007; Nagao et al. 2008; Kashikawa et al. 2012; Cassata et al. 2013), without definitive detections. These include a controversial $z = 6.6$ galaxy analyzed by Sobral et al. (2015) that displays HeII $\lambda 1640$ emission – an indicator of the hard-ultraviolet (UV) spectrum produced by Pop III stars (Tumlinson et al. 2001). Thus, to date, there has not been a confirmed observation of a galaxy dominated by the flux from Pop III stars (Bowler et al. 2016; Pacucci et al. 2017).

This may change in the near future. The soon-to-launch *James Webb Space Telescope* (JWST) is poised to greatly expand our understanding of the high-redshift universe and possibly detect the first galaxies dominated by Pop III flux. Using JWST, astronomers will be able to assemble galaxy catalogs out to $z = 10$ and beyond, and probe the era of the first galaxies (Gardner et al. 2006). However, planning for such observations requires estimating how such galaxies are distributed, and even more importantly, what fraction of galaxies as a function of magnitude and redshift will be dominated by Pop III flux – warranting spectroscopic follow-up.

For now we only have general observational clues about the history of such early galaxy formation. Using extremely deep Hubble Space Telescope (HST) observations, astronomers have been able to amass photometric galaxy catalogs out to $z = 8$ and place initial constraints on galaxy populations out to $z \approx 11$ (Ishigaki et al. 2017; Finkelstein 2016; Bouwens et al. 2015; Mason et al. 2016; McLeod et al. 2015; Coe et al. 2013; Oesch et al. 2013). While a lot of progress has been made, the latest work at $z > 8$ is hampered by small number statistics and completeness uncertainties (Livermore et al. 2017; Oesch et al. 2015; Atek et al. 2015).

Several groups have used large scale cosmological simulations and analytic models to investigate galaxy formation, the high- z luminosity function (LF) and galaxy

assembly (Somerville et al. 2012; O’Shea et al. 2015; Mason et al. 2016; Barrow et al. 2017). Others have used simulations to explore the transition between Pop III and Population II (Pop II) star formation (Scannapieco et al. 2003; Tornatore et al. 2007; O’Shea & Norman 2007; Trenti & Shull 2010; Maio et al. 2010; Zackrisson et al. 2011; Wise et al. 2012; Crosby et al. 2013; Johnson et al. 2013; Pan et al. 2013; Pallottini et al. 2014).

By definition, the first generation of Pop III stars must have formed in the primordial gas. However, an IMF lacking low-mass stars may also result from gas with metallicity below a critical threshold, Z_{crit} . The exact value of the threshold depends on whether the dominant cooling channel for the gas is the fine-structure lines of metals or dust emission (Schneider et al. 2003; Bromm & Loeb 2003; Omukai et al. 2005). While the value is poorly constrained, it is believed to be in the range $10^{-6} < Z_{\text{crit}} < 10^{-3} Z_{\odot}$.

Here make use of the work described in Sarmento et al. (2017) to track the pollution of the pristine gas at subgrid scales in high-resolution simulations of galaxy formation at high redshift. By following the evolution of the pristine gas we can estimate the fraction of Pop III stars created in regions that would otherwise be considered polluted above Z_{crit} . This allows us to present theoretical predictions for deep photometric galaxy surveys and, in particular, to characterize the fraction of Pop III flux in early galaxies. This information can guide planning for spectrographic follow-up in the search for Pop III stars, searching for their unique observational characteristics (Visbal et al. 2015).

Our approach uses a customized version of RAMSES (Teyssier 2002), a cosmological adaptive mesh refinement (AMR) simulation, to follow galaxy formation from the dawn of star formation, at $z \approx 21$, to $z = 7$. Using these simulation results we generate rest-frame UV (1500Å) galaxy luminosity functions, to demonstrate our approach is consistent with existing photometric surveys, and generate higher-redshift galaxy luminosity function for a set of JWST Near InfraRed Camera (NIR-Cam) filters, to aid in planning for future such surveys.

Furthermore, using our unique capability to track the rate of subgrid metal pollution, we trace the formation of Pop III stars in these early galaxies and model their impact on the galaxies’ flux. In doing so we are able to identify a fraction of galaxies, across a range of redshifts, that have a significant fraction of Pop III flux from young massive stars. This allows us to make predictions as to the galaxy luminosities and redshifts that are most likely to show PopIII features such as narrow HeII $\lambda 1640$ emission when they are followed up spectroscopically.

The work is structured as follows. In §2 we describe our methods including a brief discussion of the implementation of our subgrid model for following the evolution of the pristine gas fraction, our approach to halo finding and the SED models used to compute the luminosity of our stars. In §3 we show that our high redshift LF agrees with current observations and make predictions for future JWST surveys. Next we focus on an analysis of the fraction of Pop III flux emitted by early galaxies that can be used to guide the search for metal-free stars. Conclusions are discussed in §4.

2. METHODS

2.1. Simulation Setup & Characteristics

We adopt the following cosmological parameters: $\Omega_M = 0.267$, $\Omega_\Lambda = 0.733$, $\Omega_b = 0.0449$, $h = 0.71$, $\sigma_8 = 0.801$, and $n = 0.96$, based on Komatsu et al. (2011), where Ω_M , Ω_Λ , Ω_b are the total matter, vacuum, and baryonic densities, in units of the critical density, h is the Hubble constant in units of 100 km/s, σ_8 is the variance of linear fluctuations on the 8 h^{-1} Mpc scale, and n is the “tilt” of the primordial power spectrum (Larson et al. 2011).

For this study we make use of RAMSES (Teyssier 2002), a cosmological adaptive mesh refinement (AMR) simulation code that uses an unsplit second-order Godunov scheme for evolving the Euler equations. RAMSES tracks cell-centered variables that are interpolated to the cell faces for flux calculations. Flux between cells is computed using a Harten-Lax-van Leer-Contact Riemann solver (van Leer 1979; Einfeldt 1988) and the code is capable of advecting any number of these scalar quantities across simulation cells. Self-gravity is solved using the multigrid method (Guillet & Teyssier 2011) along with the conjugate gradient method for levels ≥ 12 in our simulation. Stars and DM are modeled with collisionless particles and are evolved using a particle-mesh solver with Cloud-In-Cell interpolation.

We use RAMSES to evolve a 12 Mpc h^{-1} on-a-side volume from mpgrafic (Prunet et al. 2008) generated initial conditions through $z = 7$. The initial gas metallicity was $Z = 0$, the initial H_2 fraction was 10^{-6} (Reed et al. 2005), and we define $Z_{\text{crit}} = 10^{-5} Z_\odot$. The base resolution of 1024^3 cells ($l_{\text{min}} = 10$) corresponds to a grid resolution of 11.7 comoving kpc h^{-1} , and a dark matter particle mass of $1.79 \times 10^6 M_\odot h^{-1} \Omega_{\text{DM}}$. We refined cells as they become $8\times$ over-dense, resulting in a quasi-Lagrangian approach to refinement. We allowed for up to 8 additional refinement levels ($l_{\text{max}} = 18$), resulting in an average physical spatial resolution of 45.8 pc h^{-1} . Our choice of parameters resulted in a range of star particle masses $3.2 \times 10^3 M_\odot \leq M_\star \leq 6.3 \times 10^4 M_\odot$. The highest

refinement level reached was 15. The nonlinear length scale at the end of the simulation, $z = 7$, was 47 comoving kpc h^{-1} , corresponding to a mass of $4.6 \times 10^7 M_\odot$. We did not model sink particles (black holes - BH) in our simulation since BH feedback is not likely to be significant for our very early galaxies (Somerville et al. 2008; Scannapieco & Oh 2004). We tuned the code reionization parameters to ensure that the reionization redshift occurs at $z_{\text{reion}} \approx 8.5$ as reported by the Planck Collaboration et al. (2015). Finally, all magnitudes are in the AB system (Oke & Gunn 1983).

2.2. Simulation Physics

Cooling is modeled using CLOUDY (Ferland et al. 1998) for $T \gtrsim 10^4$ K. Below 10^4 K we adopt the cooling rates from Rosen & Bregman (1995). We allow the gas to cool radiatively to 100 K, but adiabatic cooling can lower the temperature below this threshold. The UV background is derived from Haardt & Madau (1996).

We have also modified RAMSES to include a simple molecular cooling model that is important for low-temperature cooling in the pristine gas (Johnson & Bromm 2006; Prieto et al. 2008; Hirano & Yoshida 2013). Our analytic model is based on Martin et al. (1996) and provides a radiative cooling rate, Λ_r/n_{H_2} , per H_2 molecule across the range of densities encountered in the simulation. The details are found in Sarmiento et al. (2017).

Star particles (SPs) are spawned in regions of gas according to a Schmidt law (Schmidt 1959) with

$$\frac{d\rho_\star}{dt} = \epsilon_\star \frac{\rho}{t_{\text{ff}}} \theta(\rho - \rho_{\text{th}}), \quad (1)$$

where the Heaviside step function, $\theta(\rho - \rho_{\text{th}})$, allows for star formation only when the density exceeds a threshold value ρ_{th} . We have set ρ_{th} to be the maximum of $0.48 m_p \text{ cm}^{-3}$ and 150 times the mean density in the simulation. This criteria ensures that SPs are only formed in virialized halos and not in high-density regions of the cosmological flow (Rasera & Teyssier 2006; Dubois & Teyssier 2008). We set the star forming efficiency to $\epsilon_\star = 0.20$, a value that results in reasonable agreement with the observed cosmic star formation rate. The gas free-fall time is $t_{\text{ff}} = \sqrt{3\pi/(32G\rho)}$.

Each SP models a Salpeter (1955) (for polluted stars with $Z > Z_{\text{crit}}$) and a Log-Normal (for Pop III stars) initial mass function (IMF). Our SP mass resolution is dictated by the star-forming density threshold and our resolution resulting in $m_\star = \rho_{\text{th}} \Delta x^3 = 3.2 \times 10^3 M_\odot$. The final mass of each SP is drawn from a Poisson process such that is a multiple of m_\star .

A fraction of the each SP’s mass is returned to the gas in the form of supernovae (SNe). This occurs after

the 10 Myr lifetimes for the most massive stars in the IMF (Raskin et al. 2008). The impact of these SN is parameterized by the fraction of the SP mass they eject, η_{SN} , and the kinetic energy per unit mass of this ejecta, E_{SN} . We take $\eta_{\text{SN}} = 0.10$ and $E_{\text{SN}} = 10^{51}$ ergs/10 M_{\odot} for all stars formed throughout the simulation. The fraction of new metals in SN ejecta is 0.15 even though metal yields from Pop III stars are likely to have been higher (Scannapieco et al. 2003; Scannapieco 2005). We may explore different yields, and the subsequent effect on stellar enrichment, in future work.

We do not model radiative transfer nor radiation pressure. While radiation pressure from massive young stars can disrupt star formation (Wise et al. 2012; Whalen et al. 2004) it can also trigger it in dense clumps of gas (Tremblin et al. 2012; Deharveng et al. 2010). While we have not modeled its effects for this work, it will be important to characterize the effects of radiative feedback in future work.

2.3. The Pristine Fraction and the Corrected Metallicity

In order to more accurately model the fraction of Pop III stars created throughout cosmic time, we track two new metallicity-related quantities. The *pristine gas mass-fraction*, P , models the mass-fraction of gas with $Z < Z_{\text{crit}}$ in each simulation cell. The evolution of this scalar tracks the time-history of metal mixing within the cell such that when $P = 0$ the entire cell has been polluted above Z_{crit} . The scalar P_{\star} records, for all-time, the value of P in star particles at the time they are spawned and indicates the mass-fraction of the SP with $Z_{\star} < Z_{\text{crit}}$.

A simple equation can be used to describe the evolution of the pristine gas fraction in simulation cells:

$$\frac{dP}{dt} = -\frac{n}{\tau_{\text{con}}} P(1 - P^{1/n}). \quad (2)$$

This equation traces the evolution of P as a function of n and a timescale τ_{con} , which, in turn, are functions of the turbulent Mach number, M , and the average metallicity of the cell relative to the critical metallicity, \bar{Z}/Z_{crit} (Pan & Scannapieco 2010; Pan et al. 2012, 2013; Sarmento et al. 2017). Modeling the decay of the pristine gas fraction allows us to track the formation of Pop III stars, as a mass fraction of all stars created, even in cells with an average metallicity above critical.

Each SP in the simulation is tagged with the average metallicity of the medium from which it was born, $\bar{Z} \rightarrow \bar{Z}_{\star}$. Furthermore, by knowing the average metallicity, \bar{Z} (or \bar{Z}_{\star} for SPs), and the pristine gas fraction, P (P_{\star}), we can better model the metallicity of the polluted fraction

of gas (or stars). More explicitly, since \bar{Z} represents the average metallicity of a parcel of gas, and the polluted fraction, $f_{\text{pol}} \equiv 1 - P$, models the fraction of gas that is currently polluted with metals, we can use the value of f_{pol} to predict the enhanced, or corrected, metallicity

$$Z = \frac{\bar{Z}}{f_{\text{pol}}}, \quad (3)$$

of the polluted fraction of gas in each simulation cell. Similarly, Z_{\star} captures the corrected metallicity of star particles. As expected, when $f_{\text{pol}} = 1$ the corrected metallicity is the average metallicity.

The metallicity of the polluted fraction as described by Eqn. (3) is only precise when all of the metals are contained in the polluted fraction. This is true only in regions where the pristine gas is first polluted by Pop III SN. However, it is possible for some of the metals to be distributed in the pristine gas fraction defined as $0 \leq Z < Z_{\text{crit}}$. As discussed in Sarmento et al. (2017) this results in a small uncertainty in the resulting corrected metallicity of our SPs which we will ignore in this work. However, we can easily bound the correction to metallicity. While equation (3) represents the upper bound, the lower bound on the correction is

$$Z = \frac{\bar{Z} - Z_{\mathbb{P}}P}{f_{\text{pol}}}, \quad (4)$$

where $Z_{\mathbb{P}} = Z_{\text{crit}} = 10^{-5}Z_{\odot}$ is the upper limit on the metallicity of the pristine gas. If the pristine fraction has $Z_{\mathbb{P}} = 0$, as it would when polluting the primordial gas, we recover equation (3). Even when considering this uncertainty, the corrected metallicity, Z , allows us to more accurately model the metallicity of our gas and SPs than would be possible using the average metallicity alone.

Lastly we note that we do not create polluted stars when $f_{\text{pol}} < 10^{-5}$. In this case, we assume all stars formed in the cell are Pop III since only a tiny fraction of the cell is polluted with metals. While this may seem arbitrary, such a small fraction of Pop II stars do not detectably contribute to the luminosity of our galaxies over the entire redshift range analyzed.

2.4. Halo Finding

We use a modified version of HOP (Eisenstein & Hut 1998) to find star-forming regions in the simulation volume, at each redshift of interest. The standard version of HOP, distributed with RAMSES, uses the simulation's dark matter (DM) particles to find collapsed objects. However, due to the large number of DM particles in our simulation ($\approx 10^9$) it was much more efficient (in terms of both run-time and disk space) to use the SPs

to find the galaxies analyzed for this study. Our SP-based HOP (SP-HOP) algorithm finds all of the star-forming regions in our simulation, although we only analyze those with masses above $10^4 M_\odot$. Galaxies composed purely of young Pop III stars with a total mass $M_G < 10^4 M_\odot$ are not detectable by JWST at $z \geq 8$.

Many of the more massive objects found by SP-HOP consist of more than one observationally distinguishable galaxy. This is also true of the DM-based version of HOP. Hence we post-processed the halos as follows: For each SP-HOP halo we compute a mass, in stars, within a 3 kpc comoving sphere centered on the halo’s coordinates. This typically corresponds to the core of the most massive galaxy in the field. Next, we iteratively compute the mass in larger concentric spheres about this core. At each step we increase the radius by 10^{-1} arcsec – converted to a proper distance (in kpc) at the galaxy’s redshift. By using a redshift-dependent step-size based on the observational reference frame we can roughly determine the boundaries of our galaxies assuming, as is possible with the HST, that objects on the order of 0.1 arcsec apart are distinguishable. We continue increasing the radius until the fractional change in enclosed mass is less than 1 part in 10^4 . Specifically, when $\Delta M_{\text{enc},i}/M_{\text{enc},i} < 10^{-4}$ we consider the current radius to be the radius of a single galaxy. Figure 1 depicts a set of un-reprocessed SP-HOP-halos (left) and resolved galaxies (right) that result from using this procedure. The approach ensures we do not over-represent bright objects, by considering multiple galaxies as one, when computing their luminosities.

To ensure that we capture the faint-end of the luminosity function, ignoring simulation resolution effects for now, we also locate and analyze the ‘missing’ galaxies in our simulation: i.e. - those that may have been orphaned by the procedure described above. To accomplish this we collect the locations of all SP, at each redshift, that are *not* within the previously computed radii of SP-HOP galaxies. This results in a set of temporarily orphaned SP. Next, we select a star particle from this orphan list and locate all SPs within a 2 kpc, comoving, radius. If there are none, we assume the star is a galactic outlier and ignore it for the current iteration and select another star. Given a collection of SPs within 2 kpc, we compute the center-of-mass of this set and use this new location with our expanding sphere method to find the extent of the galaxy. If the resulting object has $M_G > 10^4 M_\odot$, its center-of-mass location and radius are added to the list of galaxies and stored; otherwise it is ignored. In either case, all of the object’s SPs are then removed from the orphan list and the procedure is repeated until all SPs have been processed.

2.5. Galaxy Spectral Models

The rest frame UV and filter-fluxes of our simulated galaxies are functions of the ages, metallicities, and masses of their constituent SPs. We calculate our SP luminosities using a set of simple stellar population (SSP) SED models spanning the particles’ ages and metallicity range. Our SEDs are based on *STARBURST 99* (Leitherer et al. 2014), henceforth *SB99* along with Raiter et al. (2010) and Schaerer (2003), henceforth *R10*. For the fraction of all SPs with $Z_\star \geq Z_{\text{crit}}$ our SEDs model a Salpeter (1955) Initial Mass Function (IMF) normalized to $1 M_\odot$. Since we have a precise age for each star particle, our SEDs model instantaneous bursts across the age range of SPs in the simulation. Pop III SP fractions, with $Z_\star < Z_{\text{crit}}$, are modeled using a log-normal IMF, again normalized to $1 M_\odot$ and are based on the *R10* SEDs for a zero metallicity population. The log-normal IMF is centered on a characteristic mass of $60 M_\odot$ with $\sigma = 1.0$ and a mass range $1 M_\odot \leq M \leq 500 M_\odot$. Conceptually, Pop III stars includes the mass of SPs with corrected metallicities $0 < Z_\star < Z_{\text{crit}}$ as well as the fractional mass of pristine stars, $P_\star \times M_\star$, with $Z = 0$, that represent the mass-fraction of Pop III stars born in cells with incomplete mixing. Since P_\star captures the fraction of stellar mass with $Z_\star < Z_{\text{crit}}$ the total mass of Pop III stars in each of our simulated galaxies is

$$M_{\star,\text{III}} = \sum_{n=1}^N P_{\star,n} M_{\star,n}, \quad (5)$$

where N is the total number of SPs in a galaxy and $M_{\star,n}$ is the mass of each SP.

Our *SB99* SEDs were generated over an age range of 10 kyr to 1.12 Gyr, a little less than the age of the universe at $z = 5$, in linearly-spaced steps of 0.5 Myr. Each SED covers the wavelength range $91 - 1.6 \times 10^6 \text{ \AA}$. We generated SEDs for metallicities of 0.02, 0.2, 0.4 and $1.0 Z_\odot$, for each age, using the *SB99*-implemented Padova (Girardi et al. 2000) models that include stellar and nebular emission through the onset of the thermal pulse AGB phase of stellar evolution. We supplemented the *SB99* model with a set of *R10* models for stars with $Z = 5 \times 10^{-4}$ and $5 \times 10^{-6} Z_\odot$. This allows us to interpolate over the range $Z_{\text{crit}} \leq Z_\star \leq Z_\odot$. The Pop III SEDs, by *R10*, are based on $Z = 0$ and cover the age range 10 kyr to 1 Gyr, in steps of 1 Myr. Again, the spectrum of all stars with $Z_\star < Z_{\text{crit}}$ is modeled using this SED.

In order to compute the observational flux, we redshift each of our SEDs over the range $z = 7$ to 16 applying Lyman forest and continuum absorption as described in Madau (1995). This process, along with a spectral conversion from wavelength to frequency, transforms the

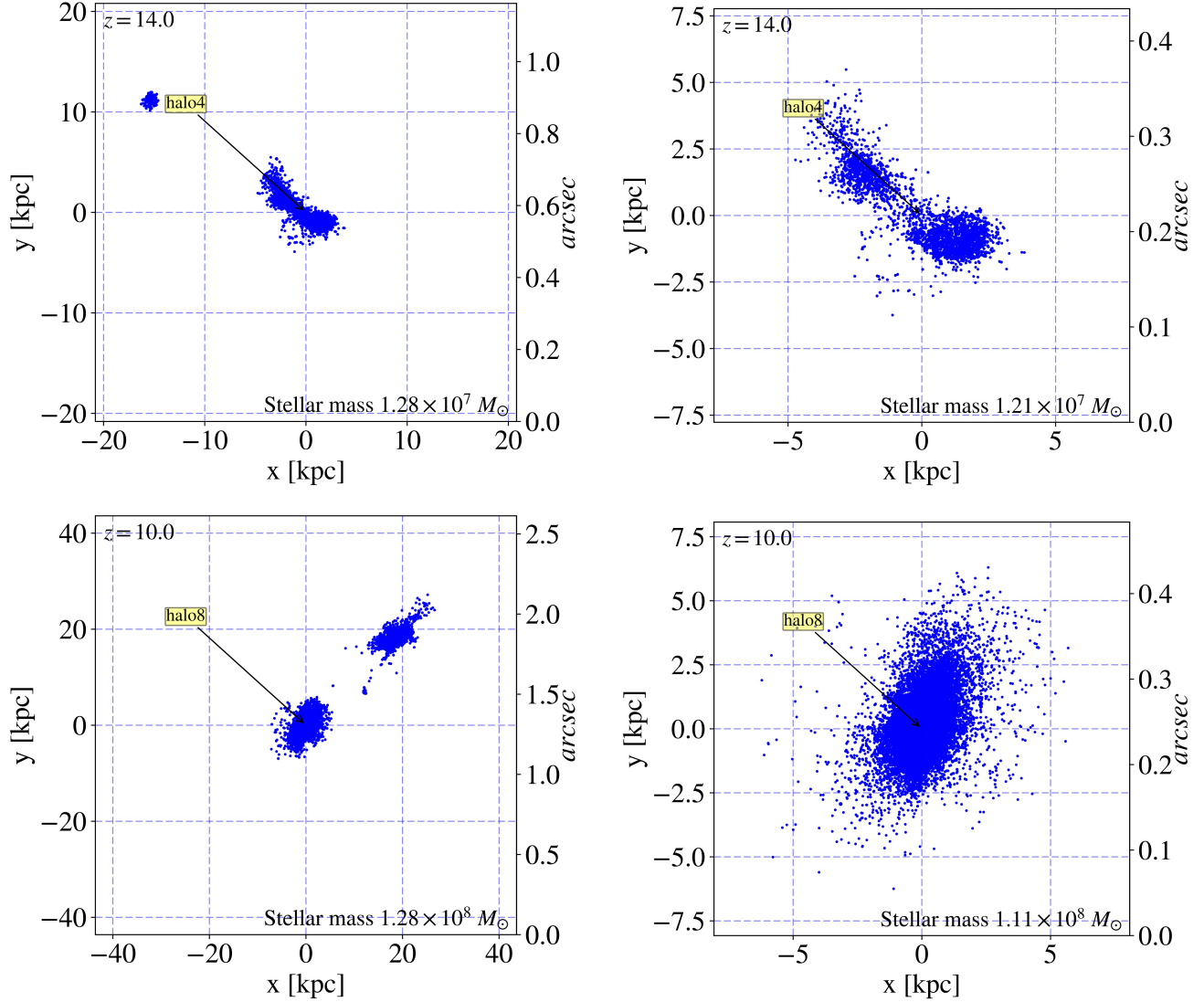


Figure 1. Scatter plots of high-redshift galaxies in our simulation. Blue points are SP locations relative to the center of the located halo (coordinate 0,0). The images on the left depict the SP-HOP-halos found by our modified SP-based algorithm. As can be seen, more than one observationally identifiable galaxy is plotted within the radius depicted. On the right, we have used our post-processing algorithm to correctly identify the larger of the two galaxies in the original field. The smaller galaxy was also identified but not depicted independently in this figure. The scale is comoving kpc and the total mass of the galaxy is identified in the lower-right of each plot. The scale on the right axes indicates the size of the field in arcseconds. Halo numbers, 4 & 8, are for reference and indicate these halos are the 4th and 8th largest, by mass, at the redshifts indicated.

Table 1. Filters modeled in this study

System	Filter names
JWST NIRCam	F150W, F200W, F277W, F356W, F444W
HST WFC3	F125W, F160W
Restframe UV	1500 Å

rest frame *SB99* and *R10* SEDs ($\text{erg/s}/\dot{A}/M_\odot$) into observational fluxes ($\text{erg/s}/H z/cm^2/M_\odot$) across the range (in redshift, age and metallicity) of our SP. Equation (6) describes this conversion from rest-frame luminosity to observational flux for objects at cosmological distances:

$$f(\nu, z) = \frac{L_\nu(\nu_e)}{4\pi D_L^2} (1+z) \mathcal{M}(\nu_o, z), \quad (6)$$

where the ν_o and ν_e are in Hz and refer to the observed and emitted reference frames, respectively, D_L is the luminosity distance and $\mathcal{M}(\nu_o, z)$ is the [Madau \(1995\)](#) Lyman absorption function. We also generate the flux at a distance of 10 pc to facilitate the generation of absolute magnitudes. This is done by setting $z = 0$, $D_L = 10$ pc and $\mathcal{M}(\nu_o, z) = 1.0$ in equation (6).

We then convolve these bolometric fluxes with the set of JWST and Hubble filters listed in Table 1. We also compute the rest-frame UV flux at 1500Å. The observational fluxes are computed as follows:

$$\mathcal{F}(R, z) = \frac{\int_{-\infty}^{\infty} f(\nu, z) R(\nu) \frac{d\nu}{\nu}}{\int_{-\infty}^{\infty} R(\nu) \frac{d\nu}{\nu}}, \quad (7)$$

where $f(\nu, z)$ is the flux at redshift z , $R(\nu)$ is the filter response function and $\mathcal{F}(R, z)$ is the resulting bandpass flux. For the rest-frame UV flux, the filter response function is the simply the Dirac delta function shifted to the observational UV wavelength, $\nu_{UV} = c/(1+z)1500\text{\AA}$, resulting in $R(\nu) = \delta(\nu - \nu_{UV})$ which simplifies equation (7) to $\mathcal{F}(R, z) = f(\nu_{UV}, z)$. The result is a set of filter-flux tables that span the range of redshifts, ages, and metallicities for a normalized star of $1M_\odot$ representing the Salpeter IMF, for $Z_\star \geq Z_{\text{crit}}$, and the log-normal IMF for $Z_\star < Z_{\text{crit}}$. This set of filter-flux tables, for each redshift, can be interpolated (in two dimensions) over the range of star particle ages and metallicities found in the simulation.

2.6. Simulated Observations

We interpolate the filter and rest-frame UV fluxes linearly, in log-space, as a function of both SP metallicity and age in order to compute the bandpass and rest-frame UV flux of our galaxies, at each redshift. The resulting

fluxes are then scaled by the mass of each SP, accounting for P_\star , and summed to compute the total flux (in each filter) for the galaxy. We then transform the filter-fluxes into AB magnitudes.

3. RESULTS

In this section we present the characteristics of our simulated galaxies. We focus on $8 \leq z \leq 16$ although some tables and figures may include data outside this range. Figure 2 depicts the star formation rate density (SFRD) for our simulation along with an observationally-derived SFRD from [Madau & Dickinson \(2014\)](#) and the SFRD from our earlier, smaller (3 Mpc h^{-1})³ and higher resolution (23 pc h^{-1}) work ([Sarmiento et al. 2017](#)). While our SFRD is higher than observations at $7 \leq z \leq 8$ it agrees well with the LF-based SFRD described by [Finkelstein \(2016\)](#) (beige region to $z = 10$). This SFRD is based on an integration of the reference luminosity functions in that work to $M_{UV} = -13$ mag. Since the observationally-based SFRDs are likely under-sampled at $z > 7$ ([Oesch et al. 2015](#)) it is more appropriate to compare our simulation to the LF-based SFRD.

The figure also depicts the Pop III SFRD (green) as well as the ‘Classical Pop III’ SFRD (red) that does not include the effects of modeling the evolution of P . We see that modeling the pristine fraction increases the SFRD for Pop III stars by an average factor of ≈ 2.1 over the redshift range $7 \leq z \leq 16$. However, we also see that the earlier work produced a Pop III SFRD a full 2 times higher than this simulation at $z > 9$. This points out the sensitivity of our results to our choice of modeling parameters such as simulation volume, resolution, star formation efficiency, star-formation density threshold, etc. As such, we plan to carry out a parameter study to better characterize and bound the effects of modeling the pristine fraction on Pop III star formation.

3.1. The Galaxy Mass-Metallicity Relation

While the galaxy mass-metallicity relation at $z > 7$ is beyond current observational work ([Zahid et al. 2013](#); [Henry et al. 2013](#); [Maiolino et al. 2008](#)), Figure 3 depicts this relationship for our simulated galaxies over the range $8 \leq z \leq 16$. The plots display the normalized probability per mass-bin, $\sum P(\bar{Z}_G/Z_\odot)/d(M_\star/M_\odot) = 1.0$, for our galaxies. This normalization clearly depicts the expected mass-metallicity trend but more importantly, for this work, the mass range of Pop III galaxies (bottom row of bins in each plot) at each redshift. Each galaxies’ average metallicity, \bar{Z}_G , is computed using the corrected SP metallicities described in Equation (3). Pop III galaxies, composed of SPs with $Z < Z_{\text{crit}}$, have been

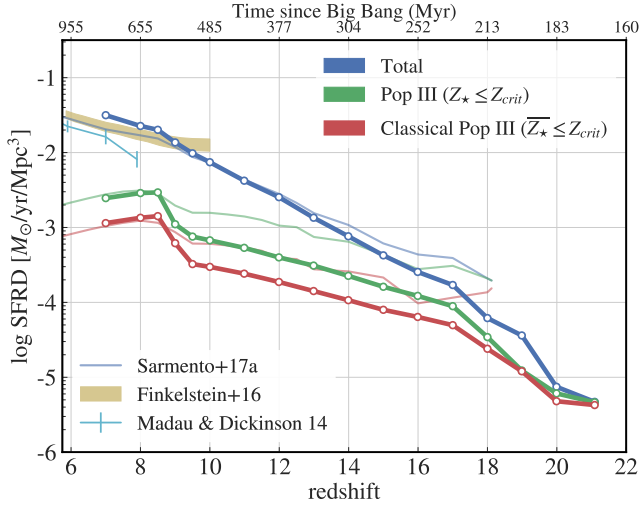


Figure 2. Our SFRD (hollow circles) along with observations by [Madau & Dickinson \(2014\)](#) and a LF-based SFRD by [Finkelstein \(2016\)](#). We have included the results from [Sarmiento et al. \(2017\)](#) to depict the sensitivity of the Pop III SFRD to our choice of parameters. While our SFRD is above observations at $z \leq 8$, it agrees well with the LF-based SFRD that incorporates galaxies down to $M_{UV} = -13$ mag.

grouped at $\overline{Z}_G < 10^{-5} Z_\odot$. While we include objects with masses $M_G \lesssim 10^5 M_\odot$ in this figure, our simulation’s resolution limits our ability to reliably model the metallicity of these proto-galaxies. A galaxy mass of $10^5 M_\odot$ corresponds to roughly 30 SPs in the best case (assuming all SPs are at the low-end of the mass range).

Taken as whole, we see that Pop III galaxies are not very massive and are comparable to the theoretical limit, $2.5 \times 10^6 M_\odot$, discussed in [Yajima & Khochfar \(2017\)](#). In fact, over the entire redshift range the most massive Pop III galaxies occur at $z = 10$ and have an average mass of $M_G = 7.32 \times 10^6 M_\odot$ – where they make up less than 1% of all galaxies with masses $M_G > 4.64 \times 10^6 M_\odot$. At lower redshift, $z = 8$, Pop III galaxies span a smaller mass-range where the most massive, again less than 1%, have $M_G \approx 3.4 \times 10^5 M_\odot$. Only a small fraction, 4%, have an average mass $M_G > 10^5 M_\odot$ at this redshift. This is likely because the rate and location of Pop III star formation is changing. The Pop III SFRD turns over at $z = 8.5$ and the Pop III fraction is no longer keeping pace with overall star formation. Since $z = 8$ is post-reionization, the majority of new star formation is likely taking place within larger, shielded galaxies – and within gas that has been polluted to levels above Z_{crit} . However, moving out to $z = 9$, we see more than 50% of proto-galaxies in the two mass-bins between $10^5 < M_G \leq 4.64 \times 10^5 M_\odot$ are Pop III – corresponding to a burst of star formation in pristine gas immediately before reionization.

The low masses of purely Pop III proto-galaxies in the range $8 \leq z \leq 11$, today’s high-redshift frontier, partially explain the difficulty in finding Pop III galaxies. However, as we shall discuss, a small percentage of young Pop III stars can contribute a significant fraction of a galaxy’s flux.

3.2. Luminosity Functions

Galaxy observations are characterized by their flux – which in turn is determined by the galaxy’s stellar populations. A small fraction of hot, young Pop III stars can contribute a large fraction of the galaxy’s luminosity. Only the Pop III stars with *age* < 3.5 Myr contribute more flux than their polluted cousins, so detecting a galaxy dominated by Pop III flux means looking for a recent starburst such that a significant fraction of the flux from the entire galaxy is coming from these types of stars. We next look at the luminosity functions and Pop III flux-fractions derived from our simulation data.

Given our total simulation volume of 4828 Mpc^3 we have data down to $\phi \approx 2 \times 10^{-4} \text{ mag}^{-1} \text{ Mpc}^{-3}$. Further, since star formation in our simulation is resolution-dependent we cannot track galaxy formation at scales below $\approx 260 \text{ pc}$, physical. While such a small proto-galaxy is likely not detectable, even by JWST, it does prevent us from characterizing the turnover at the faint-end of the LF. Additionally, several such mini-halos may merge producing larger numbers of fainter galaxies than reported here. Given this context, Figure 4 depicts the UV luminosity functions for all of our galaxies down to $M_{UV} = -14$ mag where the galaxy counts per magnitude bin begin to decrease due to the simulation’s limited resolution. We have included both observationally-derived and extrapolated [Schechter \(1976\)](#) functions by [Finkelstein \(2016\)](#) for reference: Solid grey lines indicate Schechter functions derived from observations, while grey-dashed lines are an extrapolation of the Schechter parameters – also from [Finkelstein \(2016\)](#). Schechter parameters for the observational data and extrapolations are listed in Table 2. We have also included observational data from [Bouwens et al. \(2015\)](#) and [Oesch et al. \(2013\)](#) along with data from an analysis of galaxies in the Renaissance Simulations by [O’Shea et al. \(2015\)](#). Finally, for comparison, we include galaxy models in which Pop III stars form only in gas with $\overline{Z} < Z_{\text{crit}}$ for $z \geq 13$. This is the era in which our improved method of modeling Pop III stars effects the luminosity of our galaxies. The LFs that account for Classical Pop III SPs only – where we ignore the pristine gas fraction in simulation cells – are denoted with red lines.

We note that all of our LFs at $z \leq 10$ lie above the faint-end of observationally-derived Schechter functions.

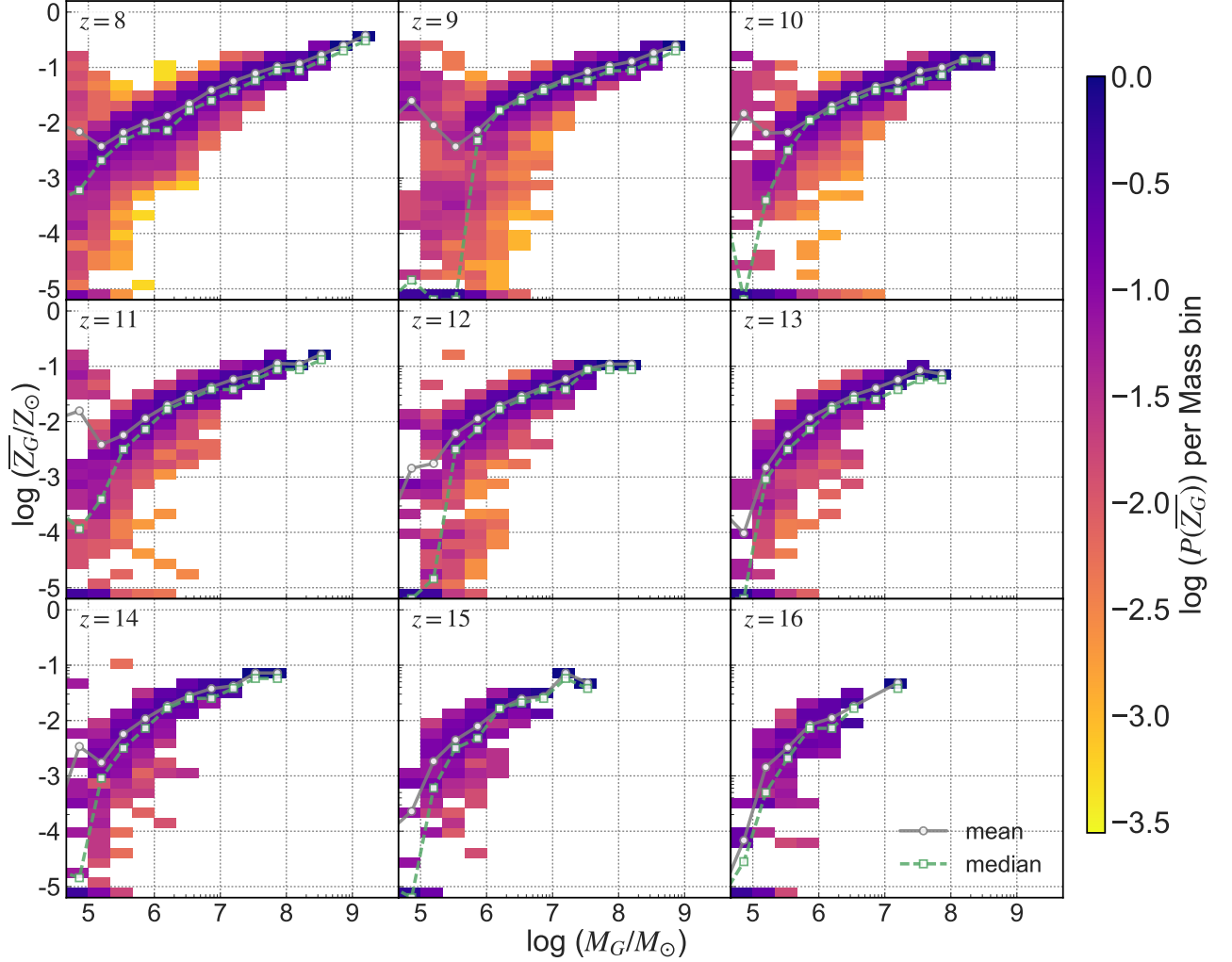


Figure 3. The normalized probability, in each mass bin, of finding a galaxy with a metallicity in the range $1 > Z_G \geq 9 \times 10^{-6} Z_\odot$ where we have binned all Pop III galaxies immediately below $Z_{\text{crit}} = 10^{-5} Z_\odot$. The grey line identifies the mean metallicity and the green dashed-line the median. Pop III galaxies with $M_G > 10^6 M_\odot$ are exceedingly rare within our simulation volume ($\approx 4800 \text{ Mpc}^3$, comoving) occurring only in the range $9 \leq z \leq 11$.

Table 2. Schechter Function Parameters

z	$\log(\phi^*)$	α	M_{UV}^*
8	-3.75	-2.13	-20.52
9	-3.94	-2.24	-20.39
10	-4.13	-2.35	-20.25
11	-4.29	-2.47	-20.11
12	-4.49	-2.58	-19.98
13	-4.69	-2.69	-19.84
14	-4.89	-2.81	-19.71
15	-5.08	-2.92	-19.57
16	-5.28	-2.03	-19.44

NOTE—Schechter function parameters for the reference lines in the luminosity function plots. Data is from Finkelstein (2016). Values at $z > 10$ have been extrapolated based on a linear fit to the parameters in that work.

However, it should be noted that data from our simulation begins at the faint-end where the observationally-derived models suffer from the greatest uncertainty. Assuming the faint-end observations are complete, our simulation produces either more galaxies per luminosity bin or brighter galaxies as compared to current models. While it is difficult to break this degeneracy given the information available, it is likely we are depicting brighter-than-average galaxies. Notably, we do not account for dust. Dust attenuation in high redshift galaxies is uncertain at best (Cullen et al. 2017; Cowley et al. 2017; Calzetti 2001) and we have not included its effects in any of our plots. However if we extrapolate work by Schaerer et al. (2015) at $z \approx 6.8 - 7.5$ to $z = 8 - 10$, we would expect $A_{UV} \approx 1.1 \pm 0.2$ of UV dust attenuation. Including this level of dust attenuation would reduce our absolute magnitudes by ≈ 1 and bring our data more in-line with the few observations at these redshifts. Additionally, our simulation represents an average-density region of the universe and our LFs in the range $-18 < M_{UV} < -14$ compares favorably with the Renaissance Simulations’ LFs at redshifts 12, 14, 15, and 16 – the redshifts where average density luminosity functions are available from that work (O’Shea et al. 2015).

Our luminosity functions closely follow the predicted faint-end slope, α , at $z > 10$. Again, these Schechter curves (grey dashed lines) are based on a linear fit and extrapolation of the trends in M^* , α , and $\log \phi^*$ using observational data over the range $4 \leq z \leq 8$. Although we have no data at the bright-end of the LF, due to our small volume, we feel our LFs are representative of galaxy populations in the range plotted.

3.3. Pop III Flux

Since we are mainly concerned with the search for Pop III stars, we focus our analysis on more detailed characteristics of our galaxies. Figure 5 depicts the normalized probability of finding a Pop III flux-fraction, as measured at 1500\AA in the rest-frame, in the range $10^{-3} \leq f_{\text{III}}/f_{\text{Tot}} \leq 1$ for our galaxies as a function of magnitude and redshift. When $f_{\text{III}}/f_{\text{Tot}} < 10^{-3}$ we have mapped the value to 10^{-3} . Note that probabilities are computed independently for each magnitude bin, as was done for the galaxy mass-metallicity relation.

The top-most row of bins in each plot represent a Pop III flux-fraction of at least 75%: $P(f_{\text{III}}/f_{\text{Tot}} \geq 0.75)$, while the next row down indicates a flux-fraction $P(0.75 > f_{\text{III}}/f_{\text{Tot}} \geq 0.50)$. Note that combining the probabilities in the 50% and 75% bins does not change the probabilities significantly from considering the 75% bins alone. Hence we use 75% as our definition of “significant Pop III flux” and a “Pop III-bright galaxy”.

Slightly more than 42% of our galaxies at $z = 9$ in the range $-19 < M_{UV} \leq -17$ (corresponding to $m_{UV} \approx 29.4$ mag) are Pop III-bright. This correlates with our observation of the increase in the SFRD at this epoch. At $z = 11$, we find $P(f_{\text{III}}/f_{\text{Tot}} \geq 0.75) \approx 40\%$ at $M_{UV} \approx -18$ mag. As we move to $z \geq 14$ we note that most of these faint objects ($M_{UV} \geq -17$ mag) are dominated by Pop III flux. This is the era of Pop III galaxies.

The results discussed so far include Pop III stars created in cells in which the subgrid turbulent mixing of metals was incomplete resulting in the enhanced Pop III SFRD we see in Figure 2. The bottom row of Figure 5 depicts the Pop III flux-fraction for our galaxies when constraining Pop III star formation to cells with $\bar{Z} < Z_{\text{crit}}$. This is the no-mixing or Classical Pop III case. When considering only the Classical Pop III SPs we see that the enhancement of the Pop III SFRD due to our subgrid turbulent mixing model, an average of $\approx 2.1 \times$ the Classical rate, is responsible for a significant amount of flux at several redshifts. For instance, considering all ‘Classical galaxies’ at $z = 8$, only 1% of the flux is from Pop III stars. However this increases to 5.6% of the flux when we track the pristine gas fraction: more than a $5 \times$ increase in flux. This result points to the importance of accurately modeling Pop III star formation since small changes in their density can significantly effect the predicted Pop III flux.

Next we consider the overall fraction of observable galaxies in the simulation that are Pop III-bright. Figure 6 identifies the joint probability that a galaxy has at least a 75% Pop III flux-fraction and $m_{UV} \leq 31.4$ mag, which we take as the limiting magnitude for the un-lensed JWST ultra-deep campaign, as a fraction of

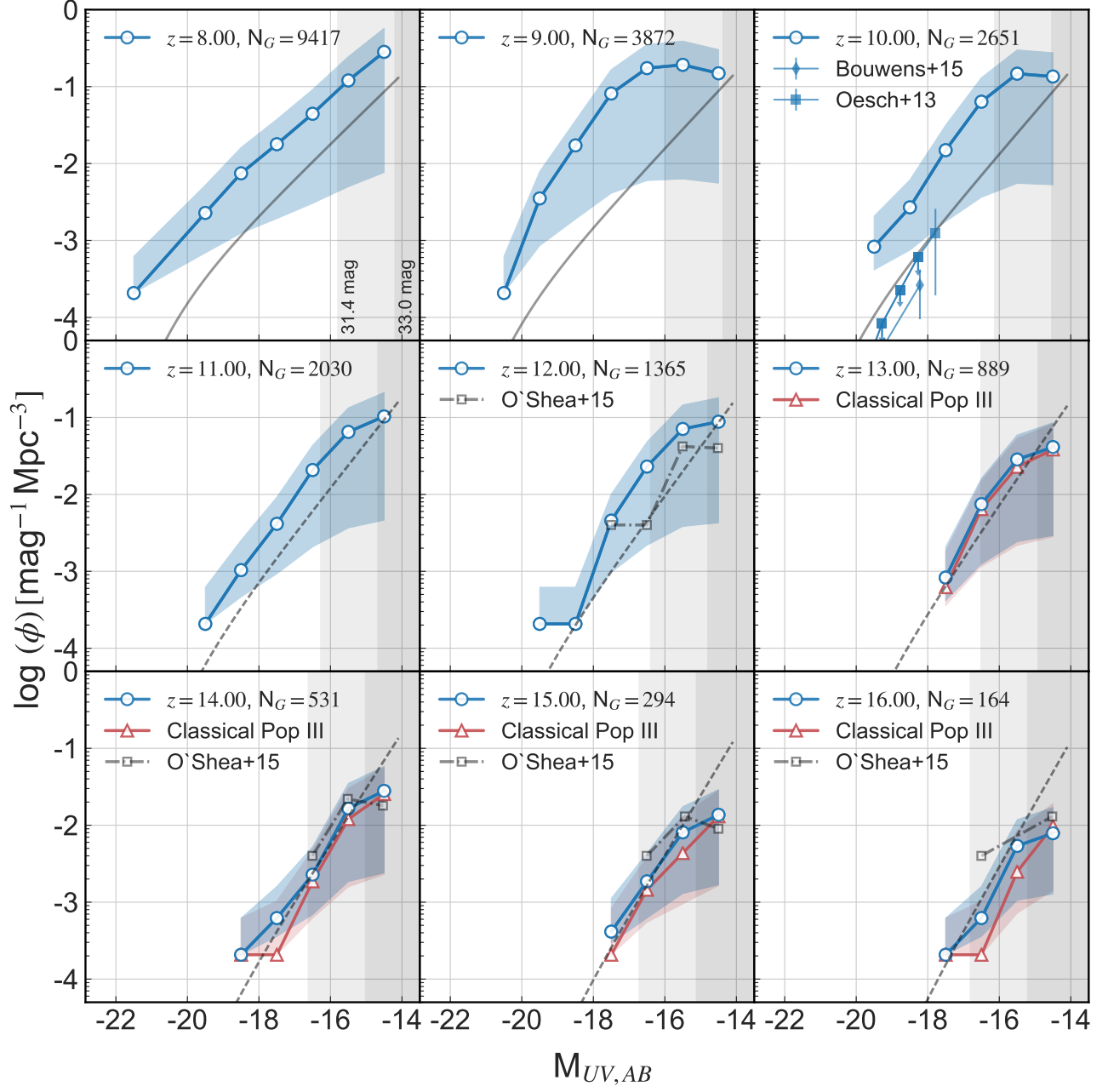


Figure 4. UV luminosity functions, with 1σ error bounds, derived from our simulation. For $z \geq 13$ the red lines model galaxies that include Pop III stars only in regions with $\bar{Z} < Z_{\text{crit}}$. Dark grey lines are Finkelstein (2016) Schechter fits. Dashed-grey lines are Schechter functions based on an extrapolation of the Schechter parameters also found in that work. For $z = 10$, we have included Bouwens et al. (2015) and Oesch et al. (2013) observational data, with error bars. For redshifts 12, 14, 15, and 16 we have included luminosity functions derived from the Renaissance Simulations by O’Shea et al. (2015). The shaded areas indicate the regions where $m_{\text{UV}} > 31.4$ mag, a likely limiting magnitude for a JWST ultra-deep campaign and $m_{\text{UV}} > 33$ mag, a likely lensing limit. Our unusually bright LF for $z = 9$ is due to the increase in the Pop III SFRD right before reionization at $z = 8.5$.

all galaxies with $m_{\text{UV}} \leq 31.4$ mag. As we would expect from current surveys, at relatively low redshift, $7 \leq z \leq 8$, the fraction of Pop III-bright galaxies is less than 5%. We again see the relatively large increase in the number of Pop III-bright galaxies at $z = 9$, immediately after a burst of Pop III star formation, where 32% of observable galaxies are Pop III-bright. This is the epoch immediately before reionization when smaller mini-halos begin to cross the star-forming mass-density threshold. It is during this epoch that we predict the largest fraction of detectable Pop III-bright galaxies. After reionization the star-forming threshold is raised quenching star formation in these mini-halos. This result points to the importance of determining the reionization redshift since most Pop III-bright galaxies are likely to be found just before it completes.

At $z = 10 - 11$ we note that between 15 and 18% of our observable galaxies are Pop III-bright. At $z = 12$, the fraction of Pop III-bright objects increases to 30% where they have an average stellar mass of $10^6 M_{\odot}$.

To illustrate the observational effects of our subgrid model, Figure 6 also identifies the fraction of observable Pop III-bright galaxies when we only account for Classical Pop III stars created in simulation cells with $\bar{Z} < Z_{\text{crit}}$. As can be seen the subgrid models' resulting enhancement to galactic Pop III flux is evident over the entire redshift range. Comparing results in the redshift range $10 \leq z \leq 12$ we note that the fraction of observable Pop III-bright galaxies is, on average, 50% higher for our subgrid model than for the Classical Pop III case. As we go deeper, the impact becomes more pronounced. At $z = 13$ the fraction of Pop III-bright galaxies increase by a factor of 3.5 over the case in which we do not track the evolution of the pristine gas fraction. At $z = 14$ and 15 our subgrid model predicts fully 50% and 20% of observable galaxies, respectively, will be Pop III-bright while the Classical case results in none of our galaxies meeting the observable Pop III-bright criteria. Again, this exemplifies the importance of modeling Pop III star formation accurately since it has a large effect on the types of galaxies we expect to detect at high redshift.

Most of the Pop III-bright galaxies form at the border of polluted areas or in regions of pristine gas away from larger halos. While our sample volume is relatively small, this result points out that Pop III-bright galaxies can be found both in relative isolation and near other, often larger galaxies with $\bar{Z}_{\text{G}} > Z_{\text{crit}}$. Once again, modeling the mixing time required to pollute the gas above Z_{crit} is important here.

By examining fainter galaxies we can find a larger fractions of galaxies with significant Pop III flux at higher redshift. Figure 6 also depicts characteristics of galax-

ies that have at least 75% of their flux coming from Pop III stars while requiring that $m_{\text{UV}} \leq 33$ mag, approximately the JWST 10x lensing limiting magnitude. With these criteria we now see that at $z = 12$ the fraction of Pop III-bright galaxies is only 21%, the result of more galaxies dominated by Pop II flux meeting the criteria $m_{\text{UV}} \leq 33$ mag. At $z = 14$ the fraction of Pop III-bright galaxies remains essentially unchanged. However, at $z = 15$ the fraction of observable Pop III-bright galaxies has jumped from 20% to 64% as a result of going to this lensing magnitude and at $z = 16$ more than 90% of galaxies are Pop III-bright. If there are enough lensing opportunities JWST should detect a large fraction of Pop III-bright galaxies at $z = 14$ and beyond.

3.4. Observational Predictions

In this section we discuss predictions for the space telescopes and filters described in Table 1. As with the rest-frame UV flux, we have not modeled dust for the results presented in this section.

The LFs derived from our simulated bandpasses are depicted in Figure 7 and cover the redshifts $z = \{10, 12, 14, 15\}$. If a particular filter or redshift is not depicted it is because there was no flux in the bandpass. For each of these plots we indicate the JWST magnitude cutoff for the deep campaign, 31.4 mag, at redshifts $z = 10$ & 15 using dark and light grey regions.

The HST F125W filter, due to Lyman forest absorption, was unable to detect any of our galaxies at $z > 10$. However, at $z = 10$ our data agrees well with the predicted Schechter faint-end slope. Using F160W we see our simulated galaxies are somewhat bright at $z = 10$, but within 1σ of the model, while our $z = 12$ data are slightly lower than predictions. This agreement with Schechter functions based on Hubble deep-field surveys is evidence that our simulation is producing reasonable results out to this redshift.

The situation is similar for the JWST bandpass filter at $1.5 \mu\text{m}$ (F150W) – our data brackets the extrapolated Schechter range. This wide-band filter straddles the Lyman- α line in the rest frame so we are seeing the attenuation of UV photons by the intergalactic medium (IGM) as we go from $z = 10 \rightarrow 12$.

The remaining data, out to $z = 12$, for the JWST filters are systematically higher than the predicted Schechter functions, although they are all within 1σ of them. We note that all of these filters sample the rest-frame in the region bluer than Lyman- α in a region where we would expect maximal dust attenuation (Calzetti 2001). This possibly explains part of the systematic brightness in relation to the predictions. In fact, a typical 1 mag reddening law would bring our LFs

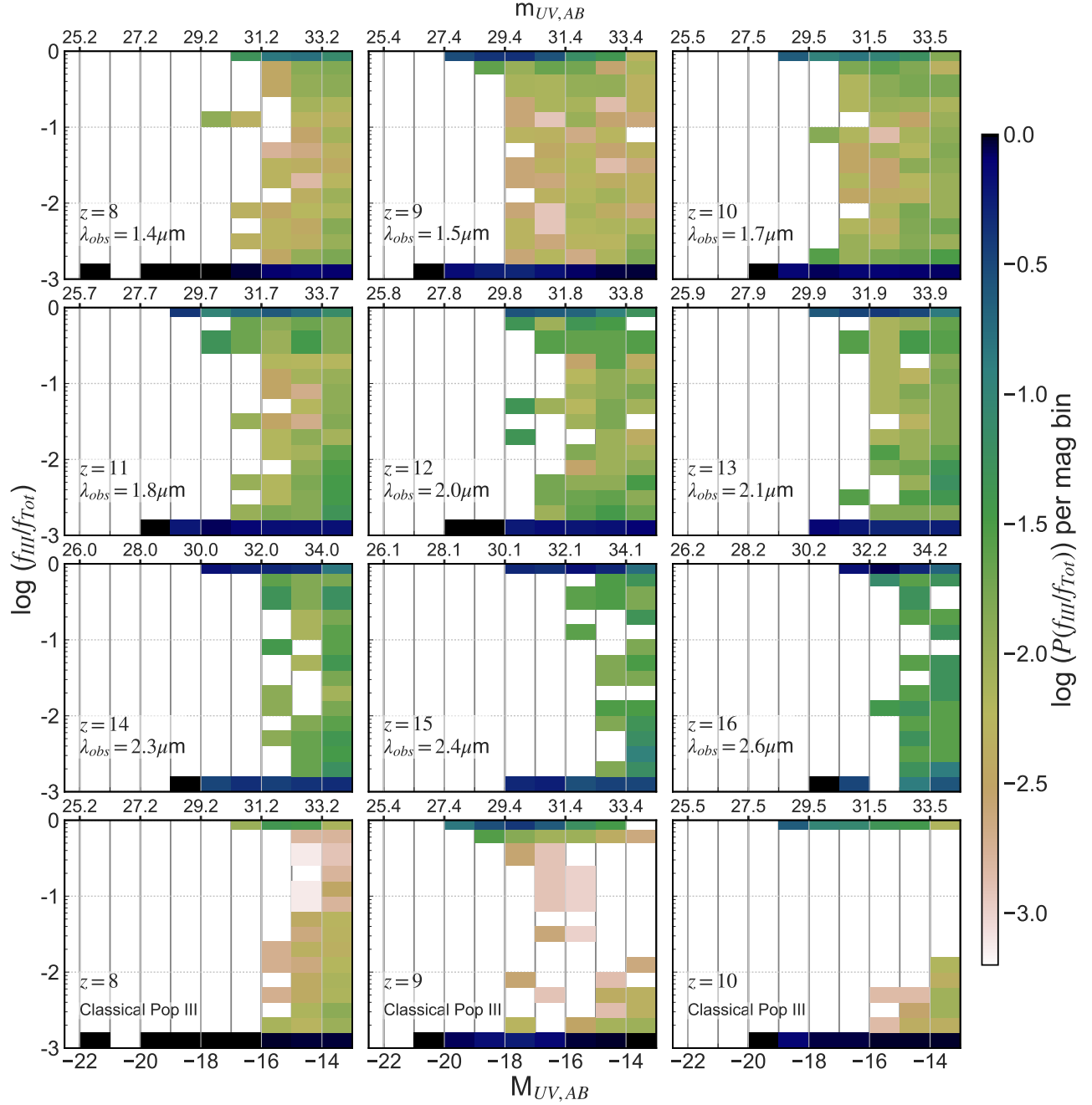


Figure 5. The normalized probability of finding a UV Pop III flux-fraction, $f_{\text{III}}/f_{\text{Tot}}$, as a function of the redshift and magnitude of our galaxies. When $f_{\text{III}}/f_{\text{Tot}} < 10^{-3}$ we map the value to 10^{-3} . Probabilities are computed independently for each magnitude bin. The top-most row of bins in each plot represent a Pop III flux-fraction of at least 75%: $f_{\text{III}}/f_{\text{Tot}} \geq 0.75$. The second row of bins represent $.75 > f_{\text{III}}/f_{\text{Tot}} \geq 0.50$. At $z = 11$, we find that 40% of galaxies at $M_{\text{UV}} = -18$ mag have $f_{\text{III}}/f_{\text{Tot}} > 75\%$. The bottom row of plots depict the Pop III flux-fraction from our galaxies when only considering stars created in cells with $\bar{Z} < Z_{\text{crit}}$, the Classical Pop III case. Modeling the evolution of the pristine gas fraction at subgrid scales results in a Pop III SRFD that is a factor of 2 increase over the classical rate and these luminous stars contribute a significant fraction of the flux of these young galaxies. Axis labels along the top axis are observed UV magnitude, m_{UV} . We identify λ_{obs} at each redshift: the wavelength of the 1500\AA reference in the observational frame.

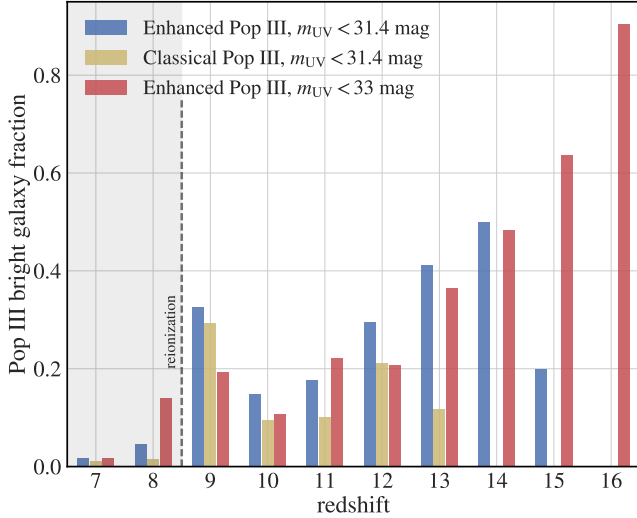


Figure 6. The blue bars indicate the joint probability of finding an observable ($m_{\text{UV}} \leq 31.4$ mag) Pop III-bright galaxy as a fraction of all observable galaxies, as a function of redshift. The yellow bars ignore the effects of our subgrid model and its enhancement to the Pop III SFRD. The resulting reduction in Pop III flux is visible across our redshift range and without it there are no Pop III-bright galaxies at $z > 13$. The red bars also depict this joint probability but for a limiting observational magnitude of $m_{\text{UV}} = 33$ mag. The burst of Pop III star formation is apparent at $z = 9$. Black lines indicate estimated 1σ uncertainties.

into good agreements with predictions. In particular, F200W and F277W sample the rest-frame flux from $0.18 \mu\text{m}$ to $0.21 \mu\text{m}$ – in the region of high dust absorption for most models. Filters F356W and F444W sample the rest-frame in the range $0.34 \mu\text{m} \leq \lambda \leq 0.40 \mu\text{m}$.

Considering our magnitude limit of $m_{\text{UV}} = 31.4$ mag, galaxies at $z > 13$ have to be brighter than $M_{\text{AB}} \approx -16.5$ to be detected by JWST and our filter fluxes for redshifts $z = 14$ & 15 bracket the limiting Schechter faint-end slope at $z = 15$. We note that none of our simulated galaxies at $z = 16$ are detectable given our assumption of a limiting magnitude $m_{\text{AB}} = 31.4$ mag. Of course, our relatively small simulation volume did not generate any of the more rare, yet bright, galaxies at these high redshifts. However, filters redder than $2 \mu\text{m}$ detect our galaxies out to $z = 15$.

4. CONCLUSIONS

We have used a large-scale cosmological simulation to study high-redshift galaxies and the prospect of finding Pop III-bright galaxies. While several of our contemporaries have done similar work (Cowley et al. 2017; Barrow et al. 2017; Liu et al. 2016; Xu et al. 2016; O’Shea et al. 2015), our approach is novel in that our models includes the enhancement to Pop III star formation caused

by the delay required to turbulently mix pollutants at subgrid scales. We find that our Pop III SFRD is approximately twice what we would have expected without modeling the subgrid pristine fraction of gas. We have analyzed more than 20,000 galaxies in our simulation volume of 4828 comoving Mpc^3 producing UV LFs and statistics on the fraction of Pop III-bright galaxies across a range of redshifts.

The current observational constraints on $z \geq 8$ LFs are uncertain at best (Finkelstein 2016; McLeod et al. 2015; Bouwens et al. 2015; Oesch et al. 2015). Determining the faint-end slope, α , is the challenge here since observations of galaxies dimmer than M^* are likely to dominate galaxy number densities at high-redshift and, more importantly, to be the home of Pop III galaxies. We find that linear extrapolations of the faint-end slope to $z > 8$, as captured in Table 2, appear reasonable to $z = 16$. While the Schechter function indicates an ever-increasing number of faint galaxies, we know that the actual LF must flatten and turn-over at some point. Even though the simulation’s resolution limits our ability to estimate this turn-over magnitude, we have determined that galaxies down to $M_{\text{UV}} = -14$ mag reasonably follow the extrapolated α . Additionally, our simulation demonstrates that M_{UV}^* , the absolute magnitude where galaxy counts begin to rapidly decay, is brighter than $M_{\text{UV}} = -17$ mag out to $z = 16$, again in agreement with linear extrapolations of current observations.

The mass-metallicity relation for our simulated galaxies follows the expected trend of increasing metallicity with increasing mass. When considering galaxies composed purely of Pop III stars, we note that they are very rare and typically have $M_G < 10^6 M_\odot$. However, the peak of Pop III galaxy formation occurs immediately before reionization where more than 50% of simulated protogalaxies are composed of Pop III stars but have stellar masses $M_G < 5 \times 10^5 M_\odot$.

Turning to Pop III-bright galaxies with at least 75% of their flux coming from Pop III stars, roughly a third of all galaxies brighter than $m_{\text{UV}} = 31.4$ mag (*observable* galaxies) are Pop III-bright at $z = 9$, immediately before reionization. Less than 5% of observable galaxies are Pop III-bright between $7 \leq z \leq 8$, after reionization. Moving to $z = 10$, the Pop III-bright fraction falls to 15% – a smaller fraction of the set of more luminous observable galaxies. Finally at $z \geq 14$, a large fraction of all galaxies are Pop III-bright, regardless of magnitude. While $m_{\text{UV}} = 31.4$ mag galaxies are likely not detectable during this epoch, we find at least 49% of galaxies at $z \geq 14$ are Pop III-bright with $m_{\text{UV}} \leq 33$ mag, a lensed magnitude limit within reach of the James Webb Space Telescope. Thus we predict that the best redshift to

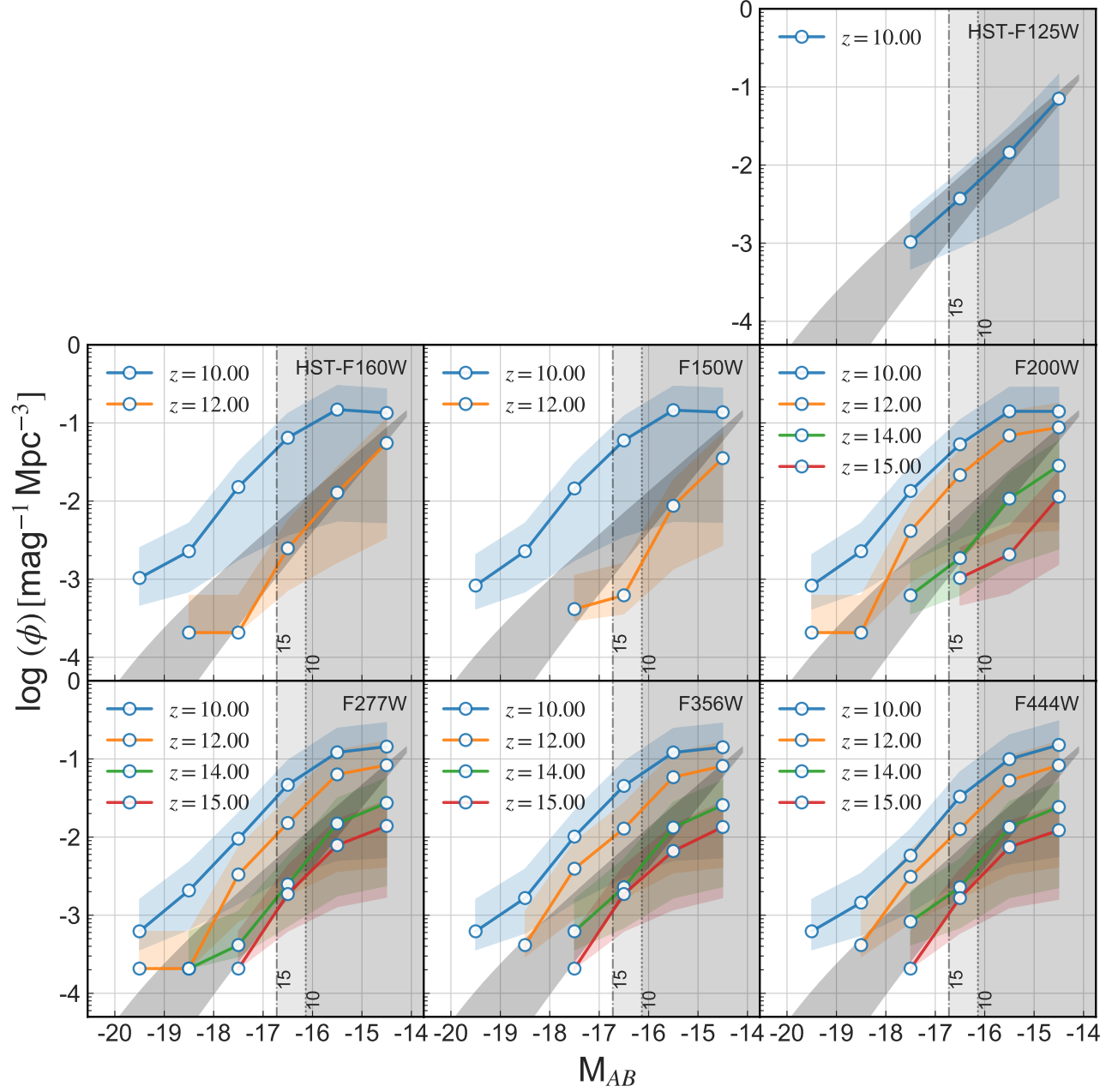


Figure 7. Luminosity functions, with 1σ error bounds, derived from our simulated galaxies convolved with our filter models across the redshift range $10 \leq z \leq 15$. The dark grey Schechter functions represent the bounding redshifts and are again from [Finkelstein \(2016\)](#) (without errors). The dark, vertical shaded areas of each plot indicate the regions where $m_{AB} > 31.4$ mag, the JWST limiting magnitude for the ultra-deep campaign, for $z = 10$ and $z = 15$. If a redshift does not appear in a plot none of our galaxies were visible in that filter. Note that we have not included dust attenuation.

search for luminous Pop III-bright galaxies is just before reionization, while lensing surveys for fainter galaxies should push to the highest redshifts possible.

Although our simulation’s enhanced Pop III SFRD has only minor implications for the luminosity functions, it does play a significant role in the fraction of Pop III flux coming from our observable ($m_{\text{UV}} \leq 31.4$ mag) high-redshift galaxies. In fact, when we consider the evolution of the subgrid pristine fraction, the fraction of observable Pop III-bright galaxies in the range $10 \leq z \leq 12$ is 1.5 times higher than in the Classical Pop III case, in which Pop III stars are only generated in cells with gas $\bar{Z} < Z_{\text{crit}}$. At $z = 13$ the Pop III-bright galaxy rate is more than 3x higher. Moreover, at $z = 14$, the Classical model predicts no observable Pop III-bright galaxies while our subgrid model predicts fully half of observable galaxies will be Pop III-bright. This emphasizes the importance of modeling Pop III star formation accurately since it has a large effect on the types of galaxies we expect to detect at high redshift.

While our subgrid model greatly improves the code’s ability to reliably produce results for a given physical model, we note that other simulations of high-redshift galaxies may make different assumptions about the relevant physics that lead to different conclusions about the observability of PopIII galaxies at $z > 10$ (e.g. Schaye et al. (2015); Jeon et al. (2014); Wise et al. (2012)). For example, a recent simulation by Jeon et al. (2015) followed the assembly of a single $10^8 M_{\odot}$ halo in a zoom simulation with a high resolution region 300 kpc^3 comoving box. They found that Pop III star formation was subdominant by $z \approx 13$ in this environment and negligible by $z = 10$. While some differences from our results are likely due to parameter choices and the type of region being simulated, they also noted that radiative transfer and related heating played a crucial role in determining their results. While our work handles cooling by molecular hydrogen along with a simple model for H_2 photodissociation, we have not yet included radiative feedback, leaving this to future work. Thus the debate is ongoing as to the relative importance of different aspects of the physics as well as the values for loosely constrained parameters.

However, our data predict good news for JWST. Although we have not considered the effects of cosmic variance with regard to JWST’s small fields-of-view (O’Shea et al. 2015; Trenti & Stiavelli 2008), or the attenuation due to dust absorption, our simulation exhibits galaxy counts per magnitude that exceed current, observationally-based predictions for filters redder than $\approx 1.6 \mu\text{m}$ through $z = 12$. At higher redshifts, $z \geq 13$, our predictions closely follow extrapolations of

the Schechter function faint-end slope and indicate detections out to $z = 15$ in filters $2.7 \mu\text{m}$ and longer.

While the simulation parameters used in this work are only a starting point for modeling the first galaxies, future work will address the sensitivity of these results across a range of values. These results will help guide future searches for Pop III galaxies.

We would like to thank Gabriela Huckabee for performing some of the research needed to reduce certain aspects of our simulation data and Mark Richardson for help with RAMSES. We would also like to thank Rogier Windhorst for helpful discussions concerning the metallicity-mass relation and the high-redshift luminosity function. This work was supported in part by the National Science Foundation under Grant No. PHY-1430152 (JINA Center for the Evolution of the Elements) and by NASA theory grant NNX15AK82G. The simulations and much of the analysis for this work was carried out on the NASA Pleiades supercomputer. We would also like to thank the NASA High-End Computing Capability support team.

Software: RAMSES (Teyssier 2002), HOP (Eisenstein & Hut 1998), pynbody (Pontzen et al. 2013), yt (Turk et al. 2011)

5. APPENDIX

In this section we briefly compare the SFRDs from two $3 \text{ h}^{-1} \text{ Mpc}^3$ simulations at different resolutions to demonstrate that the subgrid mixing model described in [Sarmento et al. \(2017\)](#) – and used herein – consistently models the formation of Pop III stars in gas with $Z < Z_{\text{crit}}$. The simulation from that work has a average physical spatial resolution of 23 pc h^{-1} resulting in the fiducial SFRD depicted in Figure 8. As expected, reducing the average physical resolution to 46 pc h^{-1} results in a slightly delayed and lower SFRD early since small-scale over-densities are ‘smoothed over’ at lower resolution. However, both the overall SFRD and the Pop III SFRD recover and reach the fiducial level of star formation by $z = 14$, demonstrating the subgrid model produces results that converge for Pop III star formation when using different resolutions.

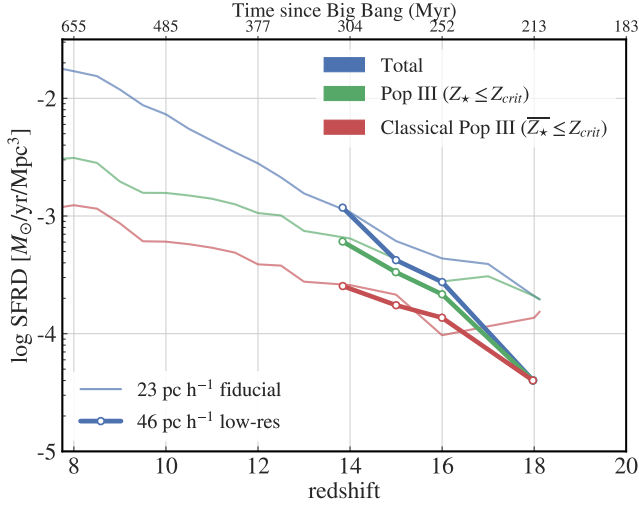


Figure 8. The SFRD for the fiducial run in [Sarmento et al. \(2017\)](#) and a run performed at 1/2 of that resolution. The subgrid model successfully recovers the overall SFRD and Pop III rate shortly after the start of star formation at $z \approx 18$ demonstrating that modeling the subgrid fraction of pristine gas generates consistent results across different simulation resolutions.

REFERENCES

- Abel, T., Bryan, G. L., & Norman, M. L. 2002, *Science*, 295, 93
- Aoki, W., Frebel, A., Christlieb, N., et al. 2006, *ApJ*, 639, 897
- Atek, H., Richard, J., Jauzac, M., et al. 2015, *ApJ*, 814, 69
- Barrow, K. S. S., Wise, J. H., Norman, M. L., O’Shea, B. W., & Xu, H. 2017, *arXiv:1701.02749*
- Berry, M., Ivezić, Ž., Sesar, B., et al. 2012, *ApJ*, 757, 166
- Bouwens, R. J., Bradley, L., Zitrin, A., et al. 2014, *ApJ*, 795, 126
- Bouwens, R. J., Illingworth, G. D., Oesch, P. A., et al. 2015, *ApJ*, 803, 34
- Bouwens, R. J., Oesch, P. A., Labbé, I., et al. 2016, *ApJ*, 830, 67
- Bowler, R. A. A., McLure, R. J., Dunlop, J. S., et al. 2016, *arXiv:1609.00727*
- Bromm, V., Coppi, P. S., & Larson, R. B. 2002, *ApJ*, 564, 23
- Bromm, V., & Loeb, A. 2003, *Nature*, 425, 812
- Bromm, V., & Larson, R. B. 2004, *ARA&A*, 42, 79
- Bromm, V. 2013, *The Intriguing Life of Massive Galaxies*, 295, 3
- Bromm, V. 2014, *Mem. Soc. Astron. Italiana*, 85, 202
- Brook, C. B., Kawata, D., Scannapieco, E., Martel, H., & Gibson, B. K. 2007, *ApJ*, 661, 10
- Caffau, E., Bonifacio, P., François, P., et al. 2011, *Nature*, 477, 67
- Calzetti, D. 2001, *PASP*, 113, 1449
- Cassata, P., Le Fèvre, O., Charlot, S., et al. 2013, *A&A*, 556, A68
- Cayrel, R., Depagne, E., Spite, M., et al. 2004, *A&A*, 416, 1117
- Christlieb, N., Bessell, M. S., Beers, T. C., et al. 2002, *Nature*, 419, 904
- Coe, D., Zitrin, A., Carrasco, M., et al. 2013, *ApJ*, 762, 32
- Cowley, W., Baugh, C., Cole, S., Frenk, C., & Lacey, C. 2017, *arXiv:1702.02146*
- Crosby, B. D., O’Shea, B. W., Smith, B. D., Turk, M. J., & Hahn, O. 2013, *ApJ*, 773, 108
- Cullen, F., McLure, R. J., Khochfar, S., Dunlop, J. S., & Dalla Vecchia, C. 2017, *MNRAS*, 470, 3006
- Dawson, S., Rhoads, J. E., Malhotra, S., et al. 2004, *ApJ*, 617, 707
- Deharveng, L., Schuller, F., Anderson, L. D., et al. 2010, *A&A*, 523, A6
- Dijkstra, M., & Wyithe, J. S. B. 2007, *MNRAS*, 379, 1589
- Dubois, Y., & Teyssier, R. 2008, *A&A*, 477, 79
- Frebel, A., Aoki, W., Christlieb, N., et al. 2005, *Nature*, 434, 871
- Einfeldt, B. 1988, *SIAM Journal on Numerical Analysis*, 25, 294
- Eisenstein, D. J., & Hut, P. 1998, *ApJ*, 498, 137
- Ferland, G. J., Korista, K. T., Verner, D. A., et al. 1998, *PASP*, 110, 761
- Finkelstein, S. L. 2016, *PASA*, 33, e037
- Gardner, J. P., Mather, J. C., Clampin, M. et al. *Space Sci Rev* (2006) 123: 485. doi:10.1007/s11214-006-8315-7
- Girardi, L., Bressan, A., Bertelli, G., & Chiosi, C. 2000, *A&AS*, 141, 371
- Greif, T. H., Glover, S. C. O., Bromm, V., & Klessen, R. S. 2010, *ApJ*, 716, 510
- Guillet, T., Chapon, D., & Teyssier, R. 2011, *Journal of Computational Physics*, 230, 4756
- Haardt, F., & Madau, P. 1996, *ApJ*, 461, 20
- Hartwig, T., Bromm, V., Klessen, R. S., & Glover, S. C. O. 2015, *MNRAS*, 447, 3892
- Henry, A., Scarlata, C., Domínguez, A., et al. 2013, *ApJL*, 776, L27
- Hirano, S., & Yoshida, N. 2013, *ApJ*, 763, 52
- Howes, L. M., Casey, A. R., Asplund, M., et al. 2015, *Nature*, 527, 484
- Ishigaki, M., Kawamata, R., Ouchi, M., Oguri, M., & Shimasaku, K. 2017, *arXiv:1702.04867*
- Ishiyama, T., Sudo, K., Yokoi, S., et al. 2016, *arXiv:1602.00465*
- Jeon, M., Pawlik, A. H., Bromm, V., & Milosavljević, M. 2014, *MNRAS*, 444, 3288
- Jeon, M., Bromm, V., Pawlik, A. H., & Milosavljević, M. 2015, *MNRAS*, 452, 1152
- Jimenez, R., & Haiman, Z. 2006, *Nature*, 440, 501
- Johnson, J. L., & Bromm, V. 2006, *MNRAS*, 366, 247
- Johnson, J. L., Dalla Vecchia, C., & Khochfar, S. 2013, *MNRAS*, 428, 1857
- Kashikawa, N., Nagao, T., Toshikawa, J., et al. 2012, *ApJ*, 761, 85
- Keller, S. C., Bessell, M. S., Frebel, A., et al. 2014, *Nature*, 506, 463
- Koekemoer, A. M., Ellis, R. S., McLure, R. J., et al. 2013, *ApJS*, 209, 3
- Komatsu, E., Smith, K. M., Dunkley, J., et al. 2011, *ApJS*, 192, 18
- Larson, D., Dunkley, J., Hinshaw, G., et al. 2011, *ApJS*, 192, 16
- Leitherer, C., Ekström, S., Meynet, G., et al. 2014, *ApJS*, 212, 14
- Liu, C., Mutch, S. J., Angel, P. W., et al. 2016, *MNRAS*, 462, 235

- Livermore, R. C., Finkelstein, S. L., & Lotz, J. M. 2017, *ApJ*, 835, 113
- Ma, X., Hopkins, P. F., Faucher-Giguère, C.-A., et al. 2016, *MNRAS*, 456, 2140
- Madau, P. 1995, *ApJ*, 441, 18
- Madau, P., & Dickinson, M. 2014, *ARA&A*, 52, 415
- Maio, U., Ciardi, B., Dolag, K., Tornatore, L., & Khochfar, S. 2010, *MNRAS*, 407, 1003
- Malhotra, S., & Rhoads, J. E. 2002, *ApJL*, 565, L71
- Maiolino, R., Nagao, T., Grazian, A., et al. 2008, *A&A*, 488, 463
- Mannucci, F., Cresci, G., Maiolino, R., Marconi, A., & Gnerucci, A. 2010, *MNRAS*, 408, 2115
- Martin, P. G., Schwarz, D. H., & Mandy, M. E. 1996, *ApJ*, 461, 265
- Mashian, N., Oesch, P. A., & Loeb, A. 2016, *MNRAS*, 455, 2101
- Mason, C. A., Trenti, M., & Treu, T. 2015, *ApJ*, 813, 21
- Mason, C. A., Trenti, M., & Treu, T. 2016, *ApJ*, 816, 46
- McLeod, D. J., McLure, R. J., Dunlop, J. S., et al. 2015, *MNRAS*, 450, 3032
- Nagao, T., Sasaki, S. S., Maiolino, R., et al. 2008, *ApJ*, 680, 100
- Norris, J. E., Christlieb, N., Korn, A. J., et al. 2007, *ApJ*, 670, 774
- Oesch, P. A., Bouwens, R. J., Illingworth, G. D., et al. 2013, *ApJ*, 773, 75
- Oesch, P. A., Bouwens, R. J., Illingworth, G. D., et al. 2015, *ApJ*, 808, 104
- Oke, J. B., & Gunn, J. E. 1983, *ApJ*, 266, 713
- Omukai, K., Tsuribe, T., Schneider, R., & Ferrara, A. 2005, *ApJ*, 626, 627
- O’Shea, B. W., Wise, J. H., Xu, H., & Norman, M. L. 2015, *ApJL*, 807, L12
- O’Shea, B. W., & Norman, M. L. 2007, *ApJ*, 654, 66
- Pacucci, F., Pallottini, A., Ferrara, A., & Gallerani, S. 2017, *MNRAS*, 468, L77
- Pallottini, A., Ferrara, A., Gallerani, S., Salvadori, S., & D’Odorico, V. 2014, *MNRAS*, 440, 2498
- Pan, L., & Scalo, J. 2007, *ApJL*, 654, L29
- Pan, L., & Scannapieco, E. 2010, *ApJ*, 721, 1765
- Pan, L., Scannapieco, E., & Scalo, J. 2012, *JFM*, 700, 459
- Pan, L., Scannapieco, E., & Scalo, J. 2013, *ApJ*, 775, 111
- Planck Collaboration, Ade, P. A. R., Aghanim, N., et al. 2015, *arXiv:1502.01589*
- Prieto, J. P., Infante, L., & Jimenez, R. 2008, *arXiv:0809.2786*
- Pontzen, A., Roškar, R., Stinson, G., & Woods, R. 2013, *Astrophysics Source Code Library*, ascl:1305.002
- Prunet, S., Pichon, C., Aubert, D., et al. 2008, *ApJS*, 178, 179
- Raiter, A., Schaerer, D., & Fosbury, R. A. E. 2010, *A&A*, 523, A64
- Rasera, Y., & Teyssier, R. 2006, *A&A*, 445, 1
- Raskin, C., Scannapieco, E., Rhoads, J., & Della Valle, M. 2008, *ApJ*, 689, 358
- Reed, D. S., Bower, R., Frenk, C. S., et al. 2005, *MNRAS*, 363, 393
- Richardson, M. L. A., Scannapieco, E., & Thacker, R. J. 2013, *ApJ*, 771, 81
- Ritter, J. S., Sluder, A., Safranek-Shrader, C., Milosavljević, M., & Bromm, V. 2015, *MNRAS*, 451, 1190
- Rosen, A., & Bregman, J. N. 1995, *ApJ*, 440, 634
- Salpeter, E. E. 1955, *ApJ*, 121, 161
- Salvadori, S., Ferrara, A., Schneider, R., Scannapieco, E., & Kawata, D. 2010, *MNRAS*, 401, L5
- Sarmiento, R., Scannapieco, E., & Pan, L. 2017, *ApJ*, 834, 23
- Scannapieco, E., Schneider, R., & Ferrara, A. 2003, *ApJ*, 589, 35
- Scannapieco, E. 2005, *ApJL*, 624, L1
- Scannapieco, E., Kawata, D., Brook, C. B., et al. 2006, *ApJ*, 653, 285
- Scannapieco, E., & Oh, P. 2004, *Bulletin of the American Astronomical Society*, 36, 94.21
- Schaerer, D. 2002, *A&A*, 382, 28
- Schaerer, D. 2003, *A&A*, 397, 527
- Schaerer, D., Boone, F., Zamojski, M., et al. 2015, *A&A*, 574, A19
- Schechter, P. 1976, *ApJ*, 203, 297
- Schneider, R., Ferrara, A., Salvaterra, R., Omukai, K., & Bromm, V. 2003, *Nature*, 422, 869
- Schaye, J., Crain, R. A., Bower, R. G., et al. 2015, *MNRAS*, 446, 521
- Sobral, D., Matthee, J., Darvish, B., et al. 2015, *ApJ*, 808, 139
- Somerville, R. S., Hopkins, P. F., Cox, T. J., Robertson, B. E., & Hernquist, L. 2008, *MNRAS*, 391, 481
- Somerville, R. S., Hopkins, P. F., Cox, T. J., Robertson, B. E., & Hernquist, L. 2008, *MNRAS*, 391, 481
- Somerville, R. S., Gilmore, R. C., Primack, J. R., & Domínguez, A. 2012, *MNRAS*, 423, 1992
- Sutherland, R. S., & Dopita, M. A. 1993, *ApJS*, 88, 253
- Teyssier, R. 2002, *A&A*, 385, 337
- Tornatore, L., Ferrara, A., & Schneider, R. 2007, *MNRAS*, 382, 945
- Trenti, M., & Shull, J. M. 2010, *ApJ*, 712, 435
- Trenti, M., & Stiavelli, M. 2008, *ApJ*, 676, 767-780

- Tremblin, P., Audit, E., Minier, V., Schmidt, W., & Schneider, N. 2012, *A&A*, 546, A33
- Tumlinson, J., Giroux, M. L., & Shull, J. M. 2001, *ApJL*, 550, L1
- Tumlinson, J. 2006, *ApJ*, 641, 1
- Turk, M. J., Smith, B. D., Oishi, J. S., et al. 2011, *ApJS*, 192, 9
- van Leer, B. 1979, *Journal of Computational Physics*, 32, 101
- Visbal, E., Haiman, Z., & Bryan, G. L. 2015, *MNRAS*, 450, 2506
- Whalen, D., Abel, T., & Norman, M. L. 2004, *ApJ*, 610, 14
- Wilkins, S. M., Bouwens, R. J., Oesch, P. A., et al. 2016, *MNRAS*, 455, 659
- Wise, J. H., Turk, M. J., Norman, M. L., & Abel, T. 2012, *ApJ*, 745, 50
- Xu, H., Norman, M. L., O’Shea, B. W., & Wise, J. H. 2016, *ApJ*, 823, 140
- Yajima, H., & Khochfar, S. 2017, *MNRAS*, 467, L51
- Yoshida, N., Abel, T., Hernquist, L., & Sugiyama, N. 2003, *ApJ*, 592, 645
- Zackrisson, E., Rydberg, C.-E., Schaerer, D., Östlin, G., & Tuli, M. 2011, *ApJ*, 740, 13
- Zahid, H. J., Geller, M. J., Kewley, L. J., et al. 2013, *ApJL*, 771, L19